ORIGINAL ARTICLE

3D-printed Biomimetic Bioactive Glass Scaffolds for Bone Regeneration in Rat Calvarial Defects

Krishna C. R. Kolan[1]*, Yue-Wern Huang[2], Julie A. Semon[2], Ming C. Leu[1]

[1]Department of Mechanical and Aerospace Engineering, Missouri University of Science and Technology, Rolla, Missouri, USA

[2]Department of Biological Sciences, Missouri University of Science and Technology, Rolla, Missouri, USA

Abstract: The pore geometry of scaffold intended for the use in the bone repair or replacement is one of the most important parameters in bone tissue engineering. It affects not only the mechanical properties of the scaffold but also the amount of bone regeneration after implantation. Scaffolds with five different architectures (cubic, spherical, x, gyroid, and diamond) at different porosities were fabricated with bioactive borate glass using the selective laser sintering (SLS) process. The compressive strength of scaffolds with porosities ranging from 60% to 30% varied from 1.7 to 15.5 MPa. The scaffold's compressive strength decreased significantly (up to 90%) after 1-week immersion in simulated body fluids. Degradation of scaffolds is dependent on porosity, in which the scaffold with the largest surface area has the largest reduction in strength. Scaffolds with traditional cubic architecture and biomimetic diamond architecture were implanted in 4.6 mm diameter full-thickness rat calvarial defects for 6 weeks to evaluate the bone regeneration with or without bone morphogenetic protein 2 (BMP-2). Histological analysis indicated no significant difference in bone formation in the defects treated with the two different architectures. However, the defects treated with the diamond architecture scaffolds had more fibrous tissue formation and thus have the potential for faster bone formation. Overall, the results indicated that borate glass scaffolds fabricated using the SLS process have the potential for bone repair and the addition of BMP-2 significantly improves bone regeneration.

Keywords: Selective laser sintering, Bioactive borate glass, *In vivo* bone formation, Porosity, Pore geometry, Scaffold architecture

***Corresponding Author:** Krishna C. R. Kolan, Department of Mechanical and Aerospace Engineering, Missouri University of Science and Technology, Rolla, Missouri, USA; kolank@mst.edu.

Received: April 2, 2020; ***Accepted:*** April 16, 2020; ***Published Online:*** April 29, 2020

Citation: Kolan KCR, Huang YW, Semon JA, *et al*., 2020, 3D-printed Biomimetic Bioactive Glass Scaffolds for Bone Regeneration in Rat Calvarial Defects. *Int J Bioprint*, 6(2):274. DOI: 10.18063/ijb.v6i2.274

1 Introduction

Since the discovery of Bioglass® by Dr. Hench in 1969, researchers have identified a wide range of glass and glass-ceramic compositions for bone repair as well as soft tissue applications[1-3]. The advantage of utilizing silicate-based bioactive glasses for bone repair is their conversion to hydroxyapatite (HA), the main mineral constituent of bone, that can readily integrate with surrounding tissue[2]. The research on bioactive glasses has evolved from traditional SiO_2 networks to highly resorbable glass compositions based on B_2O_3 networks as researchers have focused on developing borate and borophosphate glasses for biological applications due to the ability to support angiogenesis and offer faster degradation[4]. Several studies have investigated gradual replacement of SiO_2 in silicate glass with B_2O_3 and reported the effects of glass dissolution, tissue infiltration, and cell culture compatibility of the borosilicate glasses[5,6]. Borate glass is chemically less durable in comparison to silicate

glass and consequently, it degrades at a faster rate which allows quick release of calcium, boron, and other ionic dissolution products and provides rapid HA formation[7]. Hence, in this study, biomimetic borate glass scaffolds for bone regeneration in rat calvarial defects were fabricated and characterized in terms of material composition, porosity, architecture, and mechanical properties.

Among different additive manufacturing (AM) techniques, the powder bed fusion and vat photopolymerization techniques enable the fabrication of complex lattice structures mimicking natural bone architectures, which is much more difficult to achieve with material extrusion techniques[8-10]. Thus, laser powder bed fusion processes like selective laser sintering (SLS) can be used to create scaffolds with different architectures to study the effects of pore shape on the mechanical properties of scaffolds and their associated bone regenerative capacity. Several methods were proposed to create scaffold CAD models that possess a gradient of porosity, conformity, and architectures that closely mimic human trabecular bone[11-16]. Several challenges exist in the powder bed fusion-based 3D printing of ceramic/glass scaffolds with complex pores of size ranging from 100 to 600 μm because of the ceramic/glass material properties and sintering requirements[17]. In the recent past, there has been interested in the fabrication of ceramic and glass structures using the selective laser melting process with the help of high-temperature preheating of substrate[18-20]. Nevertheless, an indirect method that involves additional post-processing after green part fabrication allows for controlled structural densification avoiding glass crystallization[21,22]. Unlike metallic scaffolds, bioactive glass scaffolds degrade upon implantation *in vivo* or after soaking in simulated body fluids (SBF), thereby affecting their structural integrity. Factors that influence this outcome include, but are not limited to, bioactive glass composition, scaffold porosity, and pore geometry (which affects surface area for reaction). Therefore, investigating the effect of porosity and pore geometry on the degradation of scaffolds made with bioresorbable materials, such as bioactive glasses, could help design implants to repair diverse regions of the skeletal system with different structural and biological requirements.

The effect of scaffold architecture on mechanical properties, cell proliferation, and bone regeneration has been investigated using polymer and metallic scaffolds[23-26]. There are inconclusive reports on the influence of pore size on bone regeneration. While some reports suggested pore sizes in the range of 100 – 300 μm are beneficial for bone growth, other studies demonstrated increase bone tissue growth with pores >300 μm and up to 800 μm[27,28]. Some of these studies were performed using bioceramic scaffolds and others were performed on biopolymer and metallic (titanium-based) scaffolds that do not degrade like bioactive glass. Bone repair using scaffolds made from resorbable materials such as bioactive glasses is likely to have distinct characteristics as the scaffold properties change post-implantation in the dynamic *in vivo* environment. For example, silicate-based glasses degrade slowly even *in vivo* because of the chemical stability of the SiO_2 network. A recent *in vivo* evaluation of silicate-based glass scaffolds showed that about half of the scaffold (unconverted glass) still remained in the defect region after 6 months[29]. However, borate glass fibers used to treat a calvarial defect were reported to degrade more quickly, with most of the glass converted to HA and resulting in better bone regeneration in comparison to silicate glasses[30].

The scaffold architecture could also play an important role in *in vitro* cell proliferation, differentiation, and bone regeneration, with some studies suggesting pore curvature driven tissue growth[24,31-33]. Although these *in vitro* observations were, in general, in agreement with theoretical predictions, the influence of curvature on tissue regeneration has not been demonstrated *in vivo*. Pore geometry, pore size, and porosity are interrelated. Importantly, the resorbable nature of borate glass could further complicate the mechanism of the bone regeneration process *in vivo,* relative to more predictable bone formation in metallic, or biopolymer scaffolds.

In the present study, we hypothesized that a borate glass scaffold with biomimetic architecture would have sufficient strength and stiffness for

non-loading bone repair and increase the bone regeneration in a critical-sized bone defect. To test this hypothesis, we compared the structural and mechanical properties of the borate glass scaffolds with five different architectures, namely, cubic, spherical, x, gyroid, and diamond. Degradation of scaffolds in SBF was assessed. Subsequently, cubic and diamond architecture scaffolds were chosen to evaluate the bone regeneration in a rat calvarial defect model. Cubic architecture represented a traditional lattice design whereas diamond architecture represented a biomimetic architecture that mimics natural bone, which has previously been shown to promote cell proliferation *in vitro*[34]. The treatment groups included borate glass scaffolds with or without bone morphogenetic protein-2 (BMP-2), an established osteogenesis inducing protein in this study.

2 Materials and methods

2.1 Scaffold fabrication

Bioactive borate glass (13-93B3 glass; nominal composition in wt % – 56.6% B_2O_3, 5.5% Na_2O, 11.1% K_2O, 4.6% MgO, 18.5% CaO, 3.7% P_2O_5) with an average particle size of ~12 μm was used in this research. Borate glass particles were mixed with a polymeric binder and then dry ball-milled to obtain the feedstock powder for the SLS machine (DTM Sinterstation 2000). The binder content, feedstock preparation, and scaffold fabrication parameters established previously for silicate glass (laser power – 5 W, scan speed – 508 mm/s, scan spacing – 0.23 mm, layer thickness – 76.2 μm, 15 wt % binder) were adopted in this study[35]. The fabricated parts were heat treated in a furnace (Vulcan Benchtop, York, PA) to remove the polymeric binder and sintered at 570°C for 1 h.

2.2 Scaffold assessment

Scaffolds measuring 5 × 5 × 5 mm^3 were used for compression tests and scaffolds measuring 10 × 10 × 10 mm^3 were used to measure porosity using Archimedes method. The scaffold's pore size was measured using an optical microscope. A cross-head speed of 0.5 mm/min was used during the compression tests with a mechanical load frame (Instron 4469, Norwood, MA). Five samples in each set were used and the average values were reported with standard deviation. X-ray diffraction (XRD) analysis (Philips X-Pert, Westborough, MA) was performed on the as-received borate glass powder, sintered scaffolds, as well as the dried scaffolds after soaking in the SBF to confirm the crystalline-like formations on the scaffold surface, the amorphous nature of borate glass, and its conversion. Scanning electron microscopy (SEM) (S-570, Hitachi Co., Tokyo, Japan) was used to analyze the surface morphology of the scaffold.

2.3 Degradation tests

An established protocol was used to prepare the SBF solution[36]. Samples were ultrasonically cleaned 3 times using ethanol and then dried in an oven overnight before kept in the SBF solution (100 ml of solution was used for 1 g of the scaffold). The scaffolds were soaked in an incubator maintained at 37°C. To evaluate the scaffold degradation, compression tests were conducted on soaked scaffolds in their wet condition. At least three samples in each set were used and the average values with standard deviations were reported.

2.4 Scaffold preparation before implantation

For *in vivo* tests, cubic and diamond scaffolds were grinded to the required dimensions (~1.5 mm thick disks having 4.6 mm in diameter), ultrasonically washed thrice (5 min each) with ethanol, dried in air and then heat sterilized overnight at 250°C. Six animals were used for each treatment group and scaffolds with ~50% porosity were used for this study. Experiments were carried out with or without the use of BMP-2. Animals were randomized to different types of scaffold, based on the presence or absence of BMP-2. Scaffolds were soaked in SBF for 6 h and then dried at room temperature overnight before loading BMP-2 to roughen the surface for improved protein adhesion. BMP-2 was dissolved in citric acid (10 μg in 100 μl) and 10 μl of the solution was loaded on each scaffold

(equivalent of 1 µg per scaffold). Scaffolds were kept in the refrigerator overnight for protein adhesion before implantation. The adhesion and release of BMP-2 from borate glass scaffolds were assumed to be similar to the release of bovine serum albumin (BSA) from borate glass scaffolds fabricated using the SLS process. Therefore, the protocol of loading BMP-2 was developed based on the release of BSA from borate glass scaffolds that occurred over a period of 4 days. **Table 1** shows the experimental plan of scaffold placement in Sprague Dawley rats.

Table 1. Borate glass scaffold placement in rat calvarial defects.

Without BMP-2			With BMP-2		
Animal #	**Left side**	**Right side**	**Animal #**	**Left side**	**Right side**
1	D	D	7	D	D
2	D	D	8	D	D
3	D	C	9	D	C
4	C	D	10	C	D
5	C	C	11	C	C
6	C	C	12	C	C

C: Cubic; D: Diamond.

2.5 Surgical procedure

Animal care and use were approved by the Missouri S&T Institutional Animal Care and Use Committee. Twelve 12-week-old male Sprague Dawley rats (~350 g in body weight) were anesthetized with a 0.6 ml ketamine/xylazine (200 mg ketamine and 20 mg xylazine per 4 ml) abdominal injection. A full-thickness defect measuring 4.6 mm in diameter was created in the central area of each parietal bone using a hand drill and trephine bur (ACE Surgical Supply Co. Inc., Brockton, MA) under constant irrigation with saline solution without disturbing the dura mater. AutoClip® wound closing system (Braintree Scientific, Inc., Braintree, MA) was used for site closure and animals were given 0.2 ml of penicillin subcutaneously and ketoprofen (3 mg/kg body weight) intramuscularly post-surgery. After 6 weeks, animals were euthanized by means of CO_2 inhalation and samples from defect sites with surrounding bone were harvested for subsequent examination.

2.6 Histological processing

The harvested samples were fixed in 10% buffered formaldehyde for ~3 days, soaked in DI water overnight, and bisected in half. Samples were decalcified in Cal-Ex II simultaneous Fixative/ Decalcifier (Fisher Scientific, Pittsburgh, PA) solution by changing the solution every 2 days during the 1st week and then once every 4 days for about ~4 weeks. The samples were dehydrated with a series of ethanol solutions by a microwave dehydration technique (EBSciences H2850 Microwave Processor). Briefly, the sample temperature was set to ~37°C and the samples were heated for about 2.5 min in the microwave followed by 12.5 min of idle time. The samples were then soaked in xylene solution followed by paraffin mounting at 45°C using a paraffin mounting system (Leica EG 1150H, Buffalo Grove, IL). Specimens were cut at 5 µm thin sections and mounted on glass slides. Slides were stained with hematoxylin and eosin (H&E) and Masson's trichrome to determine the amount of new bone tissue and fibrous tissue. Optical images of stained sections were taken with an Olympus BX 50 microscope.

2.7 Histomorphometric analysis

Histomorphometric analysis was carried out using the stitched optical images (with Microsoft Image Composite Editor software) of the stained sections and ImageJ software[37]. The percentage of new bone formed in defects was evaluated from the optical images. The total defect area was defined as the region between the two boundaries formed during the drilling process. The remaining scaffold and the tissue within were identified. The newly formed bone was outlined and measured within the defect area and expressed as a percentage of the total defect area. The measurements were blinded and performed by persons with no knowledge of the treatment groups.

2.8 Statistical analysis

The data were reported as the mean ± standard deviation. Analysis of differences in means was

performed using a one-way analysis of variance with Tukey's *post hoc* test. The statistical significance was set at $P < 0.05$.

3 Results and discussion

3.1 Fabrication and structural assessment

CAD models of scaffolds with five different architectures and their unit cells are shown in **Figure 1A**. The porosity of cubic and X architectures is a function of the size of the unit cell and the diameter of the struts. In the case of spherical architecture, the porosity is a function of the diameter of the sphere subtracted from a unit cube. These three architectures represent the most commonly used scaffold designs for bone tissue engineering fabricated by AM techniques. The diamond and gyroid architectures were designed to create surfaces with constant mean curvature and to mimic natural trabecular bone architecture[38]. These surfaces were generated using open-source software called K3DSurf (http://k3dsurf.sourceforge.net/) and were converted to CAD files for fabrication (**Figure 1A**). The representative optical microscope images of scaffolds with varying porosities are shown in **Figure 1B**. **Figure 1C** shows representative scaffolds of each architecture and **Figure 1D** shows the diamond architecture scaffolds with different porosities.

Scaffolds were designed to have 50%, 60%, 70%, and 80% volumetric porosity but the measured apparent porosities (**Table 2**) were lower than the designed values. The overall deviation between designed and apparent porosities was ~19% for spherical, diamond, gyroid scaffolds, ~17% for cubic scaffolds, and ~25% for X scaffolds. The difference between the designed and apparent porosity was the most for X scaffolds and the least for cubic scaffolds. This was due to the powder particles getting stuck inside the pores during the excess powder removal from the "green body" (SLS fabricated part before post-processing). These powder particles were sintered during heat treatment, thereby reducing the overall porosity. It is recommended that this effect and the resulting difference in porosity be accounted in the designs before scaffold fabrication using the SLS process. The adhered powder particles in the green body also affected the overall scaffold pore sizes, shown in **Table 2**. Overall, scaffold pore sizes varied

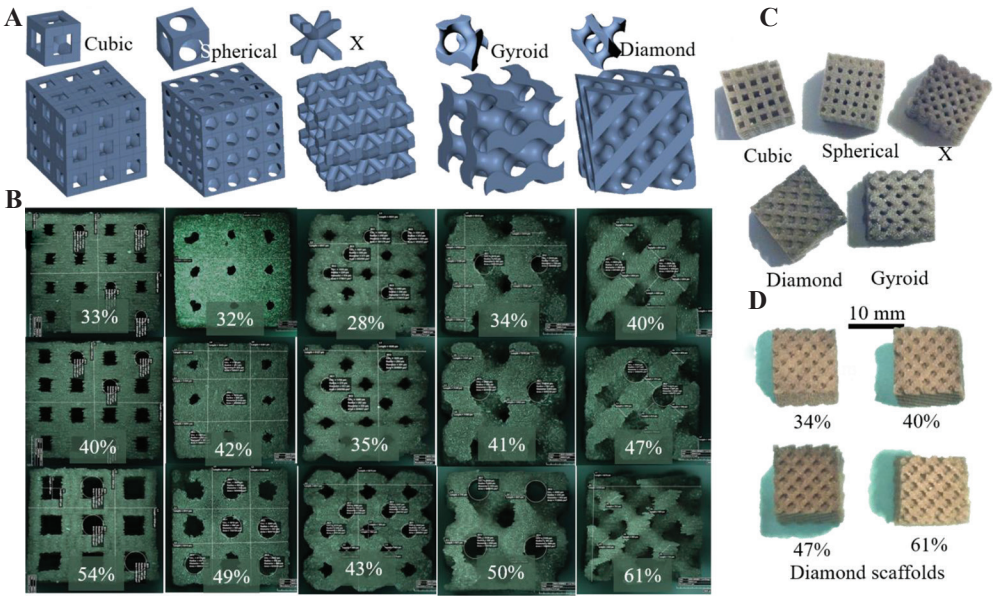

Figure 1. (A) Unit cells and scaffold architectures: Cubic, spherical, X, gyroid, and diamond, (B) representative optical images of 5 × 5 × 5 mm^3 borate glass scaffolds with corresponding architectures at three different porosities used for compression tests, (C) representative scaffold of each architecture measuring 10 × 10 × 10 mm^3 used to measure porosity, and (D) 10 × 10 × 10 mm^3 diamond architecture scaffolds at four different porosities (34% – 61%).

Table 2. Scaffold porosity and pore size.

Architecture	Designed versus apparent (%)				Measured average pore size (μm)			
	50	60	70	80	50	60	70	80
Cubic	33±2	40±2	54±1	66±3	0.5±0.02	0.7±0.02	1.0±0.04	1.3±0.02
Spherical	32±1	42±3	49±3	61±1	0.5±0.04	0.6±0.05	1.0±0.04	1.0±0.04
X	28±2	35±3	43±2	55±0	0.5±0.03	0.6±0.02	0.7±0.03	1.2±0.10
Diamond	34±2	40±1	47±1	61±1	0.8±0.01	0.9±0.01	1.0±0.04	1.2±0.05
Gyroid	34±1	41±1	49±1	60±1	0.8±0.01	0.9±0.01	1.0±0.03	1.1±0.04

between 0.5 and 1.3 mm. X architecture scaffolds had the smallest pores which are consistent with the X scaffolds having the largest difference between the designed and apparent porosities. The difficulty in removing adhered powder from the X scaffold pores of green bodies contributed to its lowest porosity and most reduced pore size. The average pore size of scaffolds designed with 80% porosity ranged from 0.9 mm to 1.3 mm, and the scaffolds designed with 50% porosity ranged from 0.5 mm to 0.8 mm. In theory, unit cell pore size varies along the Z-height, with it being the smallest at the end and the largest at the center of the unit cell. Therefore, true scaffold pore size has a range of values instead of being a constant value.

Several parameters limit the accuracy of fabricating scaffolds, including scaffold architecture, the resolution of the machine, layer thickness, binder content, and particle size. The laser spot diameter of the SLS machine was 0.45 mm and therefore, it was not feasible to fabricate scaffolds with struts smaller than this limit (<0.45 mm). The laser spot could have heated and melted particles adjacent to the scanning area, effectively reducing the designed pore size. Smaller particles are easier to remove from the green body scaffold pores, causing less deviation from the actual design. However, smaller particles require higher binder content because of the increased surface area that could increase the shrinkage and deviations between designed and fabricated parts. The amount of binder and the particle size was optimized for scaffold fabrication in our previous work[35]. One key aspect in designing the architecture was considering scaffold manufacturability. For instance, in spherical scaffolds, porosity is a function of the diameter of the sphere that is subtracted from the solid unit cube to obtain the unit cell of spherical architecture. **Figure 2A** shows unit cells of spherical and cubic scaffolds and their pore shapes and pore sizes. Decreasing sphere diameter to lower porosity would hinder the removal of powder particles from the scaffold. Hence, unit cell pores were designed to enable fabrication and removal of powder particles. The pore volume variation for cubic and spherical unit cells is shown in **Figure 2B**.

3.2 Effect of porosity and pore geometry on mechanical strength

Compressive strengths of borate glass scaffolds with different porosities are shown in **Figure 3A**. Among the five architectures investigated in this study, cubic scaffolds had the highest compressive strength (15.5 ± 1.9 MPa) and X scaffolds had the lowest strength (4.9 ± 1.2 MPa) at low porosity (~35%). The biomimetic architectures (gyroid and diamond scaffolds) had compressive strengths of 9.5 ± 2.5 MPa and 6.8 ± 1.6 MPa, respectively. The scaffold compressive strengths at low porosity were near the high end of the range of compressive strength for human trabecular bone (~2 – ~12 MPa), whereas the strengths at high porosity levels (>55%) were near the low end of the spectrum[39]. Cubic architecture scaffolds have pillars in the axial direction that carry a majority of the load in compression tests before structural failure, while the other architectures lacked a similar feature. X architecture scaffolds provided the least resistance in compression because of the 45° oriented struts. The compressive strength for all scaffold types was ~4 MPa or less at high porosities, which falls at the lower range of the trabecular bone compressive strength[39].

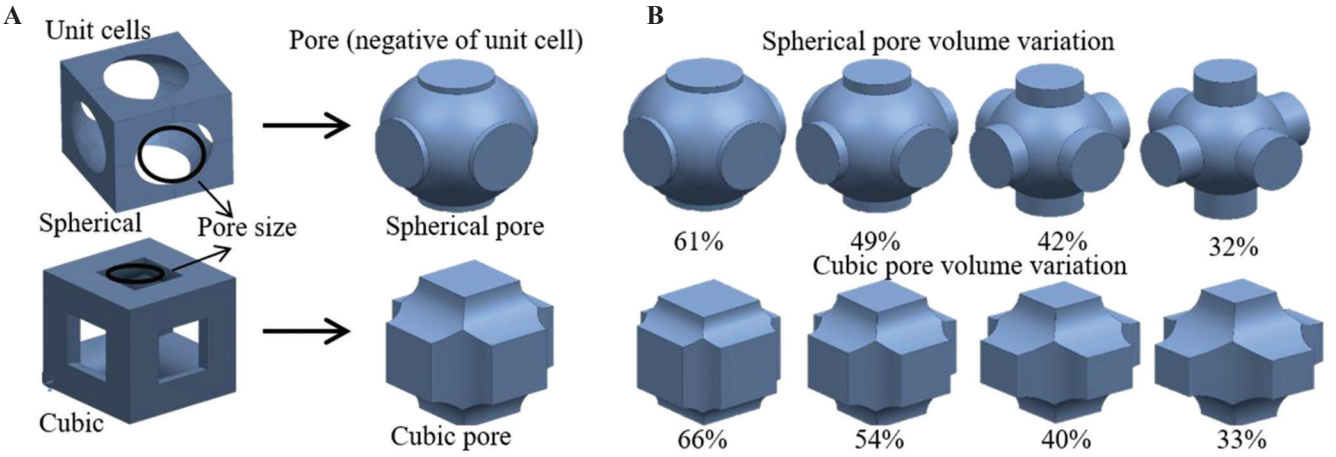

Figure 2. (A) Unit cells and pore shapes of cubic and spherical architecture scaffolds, (B) pore volume variation of spherical and cubic scaffolds with porosity. Cylindrical extensions to the spherical pores were designed to maintain sufficient pore size for powder removal from the scaffold.

Overall, the differences in scaffold compressive strength at higher porosities (>55%) were not as significant as they were at lower porosities (<35%). Architecture of scaffold contributes to cell proliferation, tissue growth, and scaffold structural integrity. Therefore, it is crucial to optimize the porosity and architecture of a scaffold, depending on the application. Another important aspect of the scaffold structural integrity is the elastic modulus during compression which measures the scaffold stiffness. Scaffolds with higher stiffness are not desired in load-bearing applications as they are known to cause stress shielding effect. However, as borate glass scaffolds fabricated using the SLS process do not possess enough structural strength for load-bearing applications and are suitable for non-load bearing applications and, the scaffold stiffness may not play a major role in bone regeneration. Nevertheless, compressive modulus values of all scaffold types are summarized in **Table 3**. Although the values are significantly less than the human trabecular bone elastic modulus (~10 GPa), the values are similar to or slightly lower than that of a rat calvaria (1.5 – 4 GPa)[39-41].

Regression models have been proposed to estimate the strength of a porous ceramic part based on the void shape[42-45]. Duckworth first proposed the exponential dependence of relative strength using the equation below[44]:

Table 3. Compressive modulus of scaffolds at designed porosities (in GPa).

Scaffold	50	60	70	80
Cubic	1.9±0.3	1.2±0.3	0.7±0.1	0.6±0.2
Spherical	1.8±0.2	1.1±0.4	0.8±0.1	-
X	1.0±0.2	0.8±0.2	0.3±0.0	-
Diamond	1.0±0.2	1.0±0.1	0.6±0.1	0.3±0.0
Gyroid	1.4±0.3	1.1±0.2	0.8±0.2	0.4±0.1

$$\sigma = \sigma_o e^{-BP} \quad (1)$$

where,

σ - Strength of porous part; σ_o - Strength of dense part;

B - Empirical constant (pore shape factor); p - Porosity fraction;

Mechanical properties of porous ceramic parts are dependent on porosity and pore shape. The results reported in the studies above showed that the B value in the equation above varied between 5 and 9 for different ceramic materials and pore shapes[43-46]. This model was adopted for structures with basic pore shapes of oblate, elliptical, and spherical[47]. Although the equation was developed for nonrandom porous mullite ceramic parts, it was reported that the compressive strength of ceramic lattice structures fit the model with independent modification of either the pore shape or the pore size[46]. In our current study, scaffolds had an open lattice structure and pores were highly

interconnected, unlike the closed pores used in the studies above. Hence, the compressive strength variation with porosity did not fit well with equation (1) and therefore, a slightly modified version of equation (1) was used to fit the data by introducing an additional empirical constant, A, as given below:

$$\sigma = A\sigma_o e^{-BP} \quad (2)$$

where,

σ - Strength of lattice; σ_o - Strength of dense part; *A, B* - Empirical constant; p - Porosity fraction;

Figure 3B shows the compressive strength versus porosity data for all scaffolds with different architectures fitted with the proposed model (equation 2). The compressive strength (σ_o), compressive modulus and density of the fully dense parts (ϕ 5 mm cylinders; 6 mm in length) were measured as 32.2 ± 6.4 MPa, 4.6 ± 0.8 GPa, and 2.16 g/cc, respectively. The equations fitted are given below:

Cubic scaffold: $\sigma = 3.9\sigma_o e^{-6.3p}$

X scaffold: $\sigma = 1.4\sigma_o e^{-6.6p}$

Spherical scaffold: $\sigma = 0.7\sigma_o e^{-2.7p}$

Gyroid scaffold: $\sigma = 2.9\sigma_o e^{-6.5p}$

Diamond scaffold: $\sigma = 1.3\sigma_0 e^{-5.3p}$

With the exception of the spherical scaffold, A value was >1 for all scaffolds and B value varied between 5.3 and 6.6 and were in agreement with other studies (B value varied between 5 and 9)[46,47]. For spherical scaffolds, A was <1 and B was <5. To verify the applicability of this trend to scaffolds made with other materials, silicate glass scaffolds were fabricated with the same five architectures and at similar porosity levels. Compressive strength data for silicate glass scaffolds were fitted to the model ($R^2 > 0.98$) to obtain the following set of equations for different architectures:

Cubic scaffold: $\sigma = 4.0\sigma_o e^{-6.7p}$

Gyroid scaffold: $\sigma = 1.1\sigma_o e^{-6.0p}$

Spherical scaffold: $\sigma = 0.6\sigma_0 e^{-3.1p}$

Diamond scaffold: $\sigma = 2.2\sigma_o e^{-8.6p}$

X scaffold: $\sigma = 1.3\sigma_o e^{-7.5p}$

The silicate glass strength, modulus, and density of the fully dense parts were 84.34 ± 5.95 MPa, 5.47 ± 1.05 GPa, and 2.3 g/cc, respectively. As can be seen from the fitted equations for silicate glass scaffolds, A was <1 and B was <5 for spherical scaffold, while A was >1 and B varied between 5 and 9 for the remaining scaffolds. This behavior of spherical scaffolds was consistent for borate glass and silicate glass scaffolds. In the formulation of equation (2), it was assumed that the empirical constants, A and B, in the model could be functions of not only the pore shape but also the pore shape variation with porosity. For cubic, X, gyroid, and diamond unit cells, the

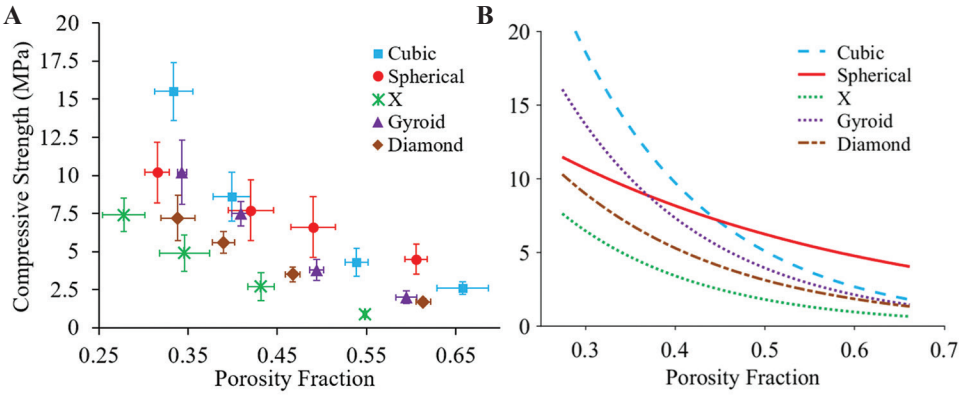

Figure 3. Compression test results: (A) Compressive strength of borate glass scaffolds with five architectures at different porosity levels. Vertical and horizontal error bars represent the standard deviations of measured compressive strength and porosities, respectively, (B) curve fitting of strength versus porosity fraction with R^2 value for all curves is >0.98.

overall pore shape remained relatively constant with increasing porosity. However, for spherical unit cell, pore shape at higher porosity (60%) is different from pore shape at lower porosity (30%). The variation of pore shapes of cubic and spherical architectures is shown in **Figure 2B**. To enable fabrication of spherical scaffolds at lower porosities, the unit cell design was modified to include cylindrical extensions to maintain the pore size resulting in pore shape variation for the spherical unit cell (**Figure 2B**). This variation in pore shape could be the reason for the different ranges of A and B values for spherical scaffolds in comparison to the remaining four architectures. To validate the above model, the data point at 32% porosity for spherical scaffolds was excluded and the remaining data for silicate glass scaffolds were fitted with the model. Following this, the A value was 1.4 and the B value was 5.0, which indicated model agreement. This suggests that empirical constants, A and B, could represent the pore shape variation in addition to the pore shape and porosity.

3.3 Scaffold degradation in SBF

The scaffolds were mechanically tested in their wet state after immersion in SBF for 1 week. The compressive strength measured for most scaffolds was about 3 MPa or less, which is near the low end of the range of compressive strength (~2 – ~12 MPa) of human trabecular bone[29]. The only exception to this was spherical scaffolds at 32% porosity, which had a compressive strength of ~4 MPa. A significant reduction in compressive modulus values for all scaffolds was also observed after 1 week, soaking in SBF. Cubic scaffolds had the highest compressive modulus ranging from 1.2 to 0.2 GPa, and X scaffolds had the lowest modulus ranging from 190 to 52 MPa, after soaking in SBF for 1 week. **Figure 4A** shows scaffold compressive strengths of all scaffold types and **Figure 4C** shows typical borate glass scaffold transformation after soaking. **Figure 4B** shows the percentage reduction in the compressive strength of scaffold types at lower (<35%) and higher (>55%) porosities. For high porosity, there was over a 90% decrease in scaffold strength, irrespective of the scaffold architecture. At low porosities, there was at least a 50% strength reduction for all scaffold regardless of their architecture. Among all scaffold types, diamond scaffolds showed a strength reduction that was consistently >80%, irrespective of the scaffold porosity. The percentage strength reduction varied from 80% to 92% for diamond scaffolds and from 76% to 94% for X scaffolds. These two scaffold architectures showed the largest strength reduction at all porosities.

SEM images were analyzed for any crystal-like formations on the bioactive glass surfaces that typically appear after immersion in SBF. **Figure 5** shows SEM images of a representative X architecture scaffold taken out of SBF after 1 week. The outer surface morphology of borate and silicate glass scaffolds at lower magnification is shown in **Figures 5A and C**, respectively. The

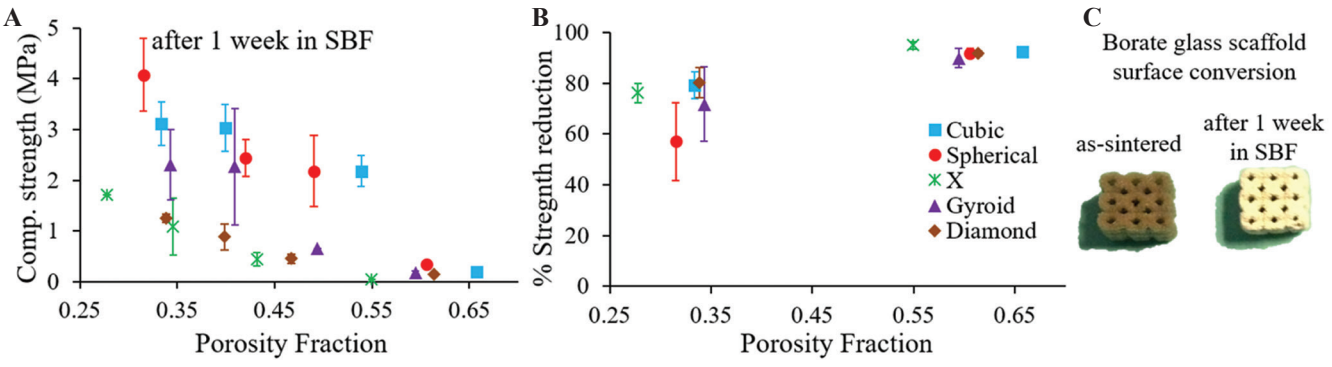

Figure 4. (A) Compressive strength of soaked scaffolds after 1 week in simulated body fluids (SBF), (B) comparison of percentage strength reduction for scaffolds with different architectures at lower and higher porosities, (C) optical image showing the physical transformation of the scaffold surface after soaking in SBF for 1 week.

corresponding higher magnification images are shown in **Figures 5B and D**. These images show the rounded spheroid-like formations on the borate glass scaffold surface, unlike needle-like crystal formations on silicate glass scaffold surface, similar to observations made by other researchers with these glasses[5,35]. The needle-like formations on silicate glass surface were confirmed as crystalline HA using XRD, whereas spheroid-like formations on borate glass surface were not confirmed to any known crystalline formations. This behavior of borate glass is not uncommon as it was reported earlier that it could take more than 60 days to form a crystalline calcium phosphate layer in SBF and it also depends on the strut size[48,49]. This was also observed in some previous work which found the presence of Ca^{2+} and PO_3^{4-} on the reacted surface of the borate glass, indicating an amorphous calcium phosphate or carbonate-substituted apatite formation[50,51].

The degradation of scaffolds made with resorbable materials depends on the material composition and porosity. Scaffold degradation is related to its surface area and the type of soaking solution (SBF in this study). Scaffolds with higher porosity degraded the most (~90% strength reduction in 1 week) irrespective of architecture. This was due to the higher surface area per unit volume and large pores, all measuring about ~1 mm (**Table 1**), that increased the efficiency of the ionic exchange with SBF and made the degradation process more rapid. To comprehend the trends in scaffolds with lower porosities, the unit cell surface area of each architecture (based on the CAD model) was plotted against the percentage strength reduction, as shown in **Figure 6**. Overall, the plot indicated a higher strength reduction with increasing surface area to volume ratio (SA/V). The SA/V data points for gyroid and diamond scaffolds form a distinguishable group from cubic, spherical, and X scaffolds. However, for a given SA/V ratio (for example, SA/V ratio of 2), diamond scaffolds show higher strength reduction in comparison to cubic and spherical scaffolds despite having a similar porosity. This indicates that the lattice structure and pore geometry do play an important role in controlling scaffold degradation, especially in the case of scaffolds made with bioresorbable materials such as bioactive glasses. Moreover, it should be noted that the actual SA/V values would be higher than the CAD values because of the surface roughness that is inherent to parts fabricated using the SLS process.

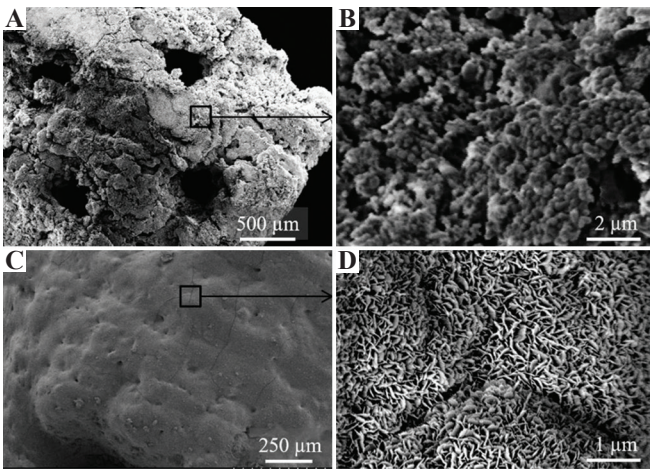

Figure 5. Scanning electron microscopy images of borate glass and silicate glass scaffolds at low and high magnifications after immersion in simulated body fluids for 1 week: (A and B) Borate glass outer surface morphology and rounded, irregular spheroid-like formations, (C and D) silicate glass scaffold surface and well defined needle-like crystalline structures at higher magnification.

3.4 New bone formation

Scaffolds were firmly integrated with the surrounding bone and pores were filled with

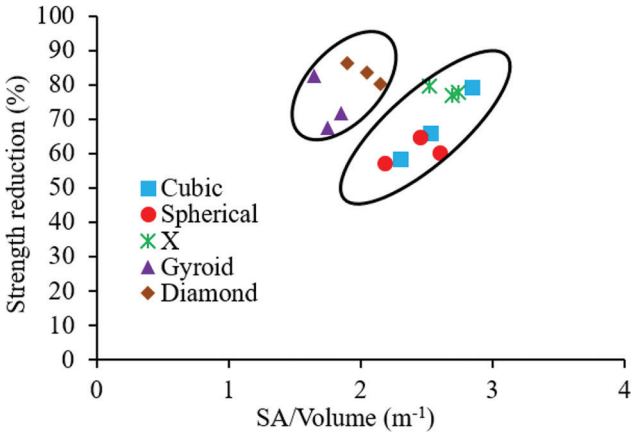

Figure 6. Percentage reduction in compressive strength of a scaffold versus the ratio of total surface area to volume of different architectures.

fibrous tissue with osteoblasts lining the pore-glass interface. **Figure 7** shows H&E stained and Masson's trichrome stained sections of full-thickness rat calvarial defect regions implanted with cubic and diamond scaffolds for 6 weeks with or without the presence of BMP-2. Although scaffolds designed at 70% porosity were planned for implantation, the apparent porosities of scaffolds used were ~54% (cubic) and ~47% (diamond) with an average pore size of 1 mm for both scaffold types. The defects treated with cubic and diamond scaffolds without BMP-2 (**Figures 7A-D**) showed no significant in new bone formation. However, small isolated pockets of new bone tissue formed inside some defects and approximately 6% of the total defect area was new bone tissue, including at the outer edges and the bottom of the defect. No statistical differences existed between scaffold types. The average overall new bone tissue formed in defects treated with cubic and diamond scaffolds as a percentage of the total defect area was 5.8 ± 1.0% and 6.2 ± 1.7%, respectively (**Figures 7A-D and 8**). In contrast, a significant amount of new bone tissue formation was observed in defects treated with cubic and diamond scaffolds loaded with BMP-2 (**Figures 7E-H and 8**). New bone tissue formed in defects implanted with cubic and diamond scaffolds occupied 39.9 ± 15.1% and 37.1 ± 13.8% of the total defect area, respectively. After normalization based on the scaffold porosities, the percentage of new bone tissue formed in cubic and diamond scaffolds was ~74% and ~79%, respectively. Despite the higher normalized bone formation in diamond scaffolds, the result was not statistically significant ($P = 0.8$).

Magnified images of the H&E stained sections of defects treated with borate glass scaffolds (cubic and diamond) without BMP-2 are shown in **Figure 9**.

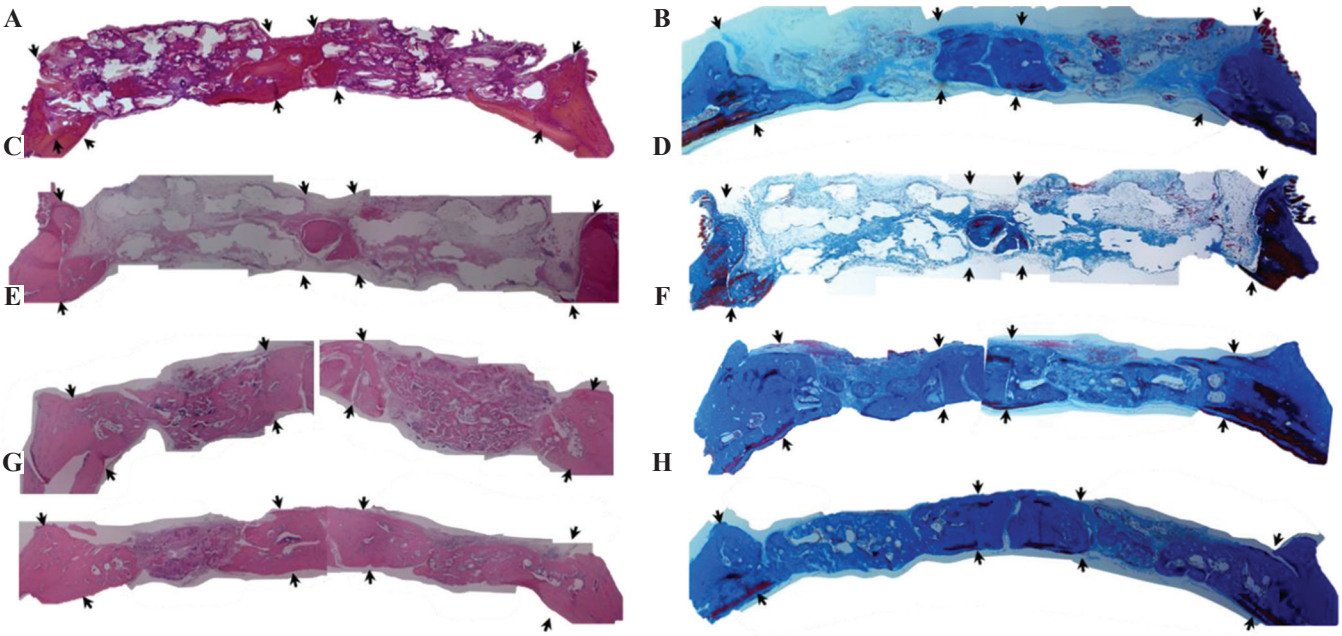

Figure 7. Hematoxylin and eosin stained sections (left) and Masson's trichrome stained sections (right) of calvarial defect regions with four different treatment groups: (A) Cubic scaffolds without bone morphogenetic protein 2 (BMP-2), (B) Cubic (left) and Diamond (right) scaffolds without BMP-2, (C and D) diamond scaffolds without BMP-2, (E and F) cubic scaffolds with BMP-2, and (G and H) diamond scaffolds with BMP-2. The arrows in the pictures point to the borders of the defect region. Dense color (pink in H&E and blue in trichrome) in sections indicates mineralized bone tissue, white/background color indicates remaining scaffold in the defect region. Red/maroon color in trichrome stained sections indicates new bone. There was no significant new bone tissue formation in defects treated with scaffolds without BMP-2. Defects treated with "scaffolds and BMP-2" show significant new bone formation. The difference in tissue formation between cubic and diamond scaffolds even with BMP-2 was not significant.

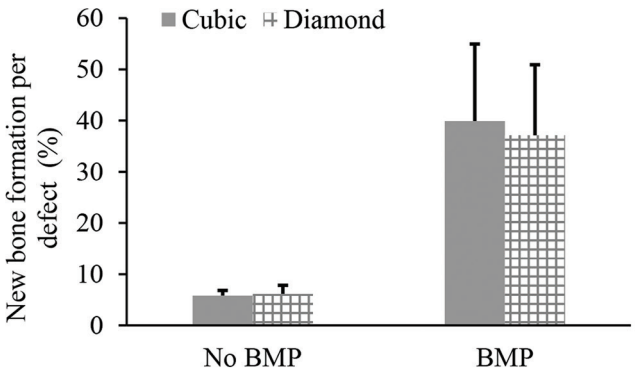

Figure 8. Percentage of new bone tissue formation in cubic and diamond scaffolds quantified based on the total defect area. The bone growth between scaffold designs with or without bone morphogenetic protein 2 (BMP-2) was not statistically different. The bone formation in defects treated with BMP-2 was statistically significant ($P = 0$).

Figures 9A and B show the tissue formation inside the diamond and cubic pores. In both cases, new bone tissue formation can be observed at the edges of the defect and in pores that are present on the underside of the defect (just above dura matter), as shown in the inset images. In addition, more mature dense fibrous tissue was formed in diamond pores in comparison to cubic pores (**Figures 9C and D**). There was a high density of osteoblasts lining the diamond scaffold surface, seen as dark purple stained cells, and indicated by arrows in **Figure 9A**. However, this was not apparent in cubic scaffolds (**Figure 9B**). Magnified images of the osteoblasts lining the scaffold surface, newly formed bone tissue, and fibroblasts in the connective tissue are shown in **Figures 9C and D**. Qualitative assessment of H&E stained sections and trichrome stained sections indicated a higher fibrous connective tissue in the diamond pores in comparison to the cubic pores. **Figures 9E and F** show new mineralized bone in pores and dense connective tissue yet to become bone. The presence of dense connective tissue and marrow-like pockets in those regions indicates the presence of endothelial cells which enable blood vessel formation and new bone tissue formation. Longer treatment duration (>6 weeks) could have resulted in significantly higher bone formation in

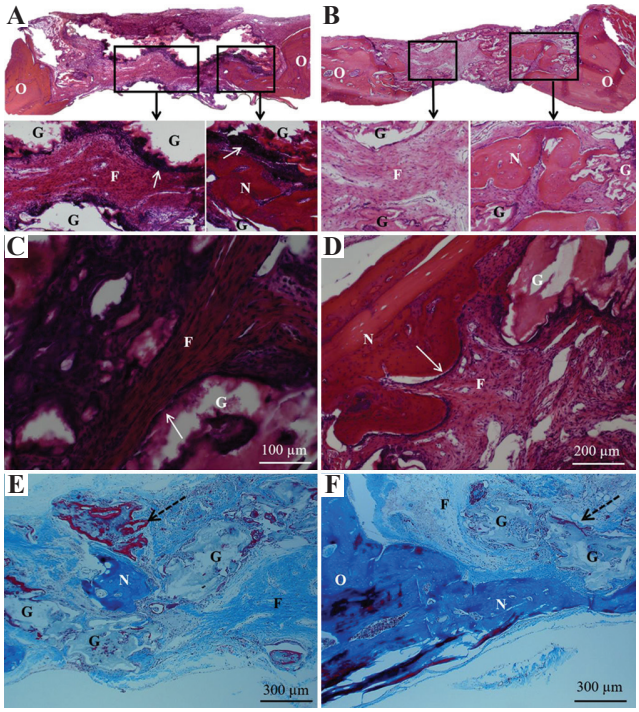

Figure 9. Histological sections of defect regions treated without bone morphogenetic protein 2 after 6 weeks. (A) Hematoxylin and eosin (H&E) stained sections of diamond scaffold, (B) H&E stained sections of cubic scaffold with the inset figures showing fibrous tissue in the pores and arrows indicating osteoblast cells lining the edges of the diamond glass scaffold strut, (C and D) magnified images of different regions of diamond scaffold showing fibrous connective tissue, newly formed bone tissue, and remaining glass, (E) Masson's trichrome stain showing pocket of mineralized bone tissue in the pore and the new bone tissue (red) surrounding the glass filament indicated by dotted arrow, (F) Trichrome stain showing mineralized bone tissue formed adjacent to host bone tissue and from the bottom side of the defect (above dura matter). N – new mineralized bone, O – original host bone, G – remaining glass, F – fibrous connective tissue.

diamond scaffolds in comparison to cubic scaffolds based on the maturity of the fibrous tissue.

Our results showed significant new bone formation in scaffolds treated with BMP-2. Uncontrolled release or high doses of BMP-2 can result in negative consequences, including tumor formation and undesired bone growth in

soft tissue[52,53]. As expected, addition of BMP-2 significantly increased new bone formation to almost 40%, based on the total defect area, and almost filled the entirety of the pores. Our results are consistent with a recent study that showed the addition of BMP-2 at the same concentration (1 μg per defect) to defects treated with HA microspheres for the same time frame also created approximately 40% new bone in a 4.6 mm diameter rat calvarial defect[54]. The above study investigated the role of relaxin, a pregnancy hormone, to control and enhance BMP-2 release to reduce the need for high concentrations of BMP-2. It was reported that the addition of 0.05 μg of relaxin to 0.5 μg of BMP-2 induced higher bone formation compared to 1 μg of BMP-2 alone per defect. In the future, a combination of relaxin and BMP-2 together with biomimetic architecture (such as diamond) could further enhance bone regeneration and repair.

As new bone formation was about 6% for both scaffold types without BMP-2, the results obtained in this study are largely in agreement with *in vivo* assessments using borate-based bioactive glasses by other researchers. **Table 4** concisely summarizes *in vivo* results using doped and undoped borate glasses. The implantation time for most studies was 8 or 12 weeks, though one study had a 6-week time point to evaluate the bone growth in defect regions using material extrusion 3D-printed scaffolds and reported approximately 6% new bone formation[55]. The material extrusion 3D-printed scaffolds had pores in the range 150 – 300 μm unlike the 1 mm pores of the cubic and diamond scaffolds used in this study. Other studies mentioned in **Table 4** utilized scaffolds made with polymer foam replication technique, freeze-drying technique, and pressed short fiber technique that have significantly smaller pore sizes, thinner strut diameters, and higher porosities. The amount of bone formation in terms of defect region was reported in the range of 9 – 28% after 12 weeks of implantation. A relatively higher amount of bone formation (up to 30%) was reported when scaffolds were made with copper and zinc doped borate glass. Higher bone growth for all the above scaffolds could be due to smaller pore size range and higher porosities compared to the scaffolds used in this study, which were limited by the laser spot size of the SLS process. The role of pore size is not completely understood as there exist reports with mixed results when using scaffolds with a range of pore sizes for bone regeneration[28]. While some studies have reported that average pore sizes in the range of 100 – 300 μm are effective for bone tissue growth, others have suggested large pores in the range of 600 –1000 μm are better for tissue growth[56,57]. Another study suggested a nonlinear effect of pore size on bone tissue regeneration for

Table 4. In vivo assessment of borate-based bioactive glasses for bone regeneration.

Study	Scaffold type	Defect and treatment duration	Porosity (%) and pore size (μm)	New bone formation
Gu *et al*.[55,58]	3D-printed grid-like and pressed short fibers	Φ4.6 mm rat cranial – 6 and 12 weeks	47 and 150 – 300 (grid-like) 58 and 50 – 550 (pressed fibers)	Grid-like 6% (6 weeks) 9% (12 weeks) pressed fibers 20% (12 weeks)
Bi *et al*.[30]	Pressed short fibers	Φ4.6 mm rat cranial – 12 weeks	58 and 50 – 500	15%
Bi *et al*.[59]	3D-printed grid-like and freeze drying	6 mm femur 12 weeks	50 and 140 – 250 (grid-like) 47 and 50 – 150 (freeze drying)	26% (grid-like) and 28% (freeze drying)
Wang *et al*.[60,61]	Polymer foam replication	Φ5.0 mm rat cranial – 8 weeks	80 – 89 and 200 – 400	16% (undoped) 29% (Zn doped) 30% (Cu coped)
This study	SLS	Φ4.6 mm rat cranial – 6 weeks	47 – 54 and 1000	6% (no BMP-2) 40% (BMP-2)

polymer scaffolds with 100 – 300 μm pores having an accelerated effect during the first 4 weeks which quickly fell off after 8 weeks of implantation[27]. If that was the case, grid-like borate glass scaffolds with 150 – 300 μm pores should have higher bone formation within 6 weeks in comparison to SLS scaffolds with 1 mm pore size used in this study. Since this was not observed, nonlinear effects of pore sizes on bone regeneration might not be the case for bioresorbable material scaffolds. The qualitative comparison of H&E stains reported in other *in vivo* studies (**Table 4**) showed that bone formation was mainly through the infiltration of fibrous tissue and initiated from the dura mater side of the scaffold. This is in strong agreement with our study. In addition, the quantification of bone growth as 6% in our study compared to 15% in other studies could be subject to a large deviation.

In our previous study, diamond and gyroid architecture scaffolds made with silicate glass showed significant cell proliferation *in vitro* in comparison to cubic scaffolds[34]. Nevertheless, a significant difference in *in vivo* bone growth for diamond scaffolds versus cubic scaffolds was not observed in the current study. However, qualitative analysis indicated a more mature fibrous tissue in defects treated with diamond scaffolds. While the fibrous tissue in the diamond scaffold appears to have osteocytes, indicating that it has almost transformed into new bone, while the fibrous tissue from the central region of the cubic scaffold appears to be soft tissue. This indicates that it would take longer to form new bone within the cubic scaffold in comparison to the diamond scaffold. Faster maturation of fibrous tissue in the diamond scaffold could be attributed to the curvature that drives the fibrous tissue, and thereby osteoblasts and osteocytes, to orient and adapt to the pore geometry. A scaffold's mechanical properties are known to influence cell proliferation, differentiation, and bone regeneration[62]. However, the mechanical properties could not be a major factor in a calvarial defect model because it is not for load-bearing application, and studies showed no apparent correlation between scaffold compressive modulus, strength, and bone formation (**Table 4**). It is likely that scaffold material (e.g. silicate glass, borate glass, or HA), pore size, porosity, and architecture play a more important role than strength and modulus in a calvarial defect model. Moreover, there was no significant difference in compressive strength and modulus of cubic (4.3 MPa and 0.7 GPa) and diamond (3.5 MPa and 0.6 GPa) scaffolds used for *in vivo* assessment in this study. Therefore, the difference in bone and fibrous tissue formation is more likely due to architecture.

This study demonstrated the fabrication of biomimetic borate glass scaffolds using the SLS process. The faster degradation of borate glass scaffolds was likely because of the increased surface area associated with the SLS part surface roughness. After immersion in SBF for 1 week, SLS borate glass scaffolds showed a 60% – 90% reduction in strength, depending on the architecture. This data provide an opportunity to design an implant to repair defect sites based on the strength requirements of the skeletal region. This shows the potential of the laser powder bed fusion process for bone repair by utilizing a combination of architecture, porosity, and choice of bioactive glass for scaffold fabrication. For example, diamond architecture could be the choice for an implant fabricated with a bioactive glass having a slower degradation rate (such as silicate glass) as diamond scaffolds degrade faster and have the potential to provide more bone regeneration *in vivo*. In a similar fashion, if high structural integrity is needed for tissue repair in a load-bearing bone, a lower porosity design using a cubic or spherical architecture could be the best option to slow down degradation. The laser powder bed fusion process can be used to manufacture bioactive glass scaffolds for bone repair with controlled degradation by selecting the appropriate geometric design and material combinations.

4 Conclusions

Borate-based bioactive glass scaffolds with different porosities and pore sizes were fabricated using the SLS process, with scaffold porosities varying from 30% to 60% and pore sizes varying from 0.5 to 1.2 mm. Scaffold strength and

degradation *in vitro* are dependent on porosity and architecture. Among the five different architectures considered in this study (cubic, spherical, x, gyroid, and diamond), cubic scaffolds provided the highest compressive strength (16 MPa) at lower porosities (<35%) and spherical scaffolds had the highest strength (4 MPa) at higher porosities (>60%). Gyroid and diamond scaffolds recorded greater strength reduction after 1-week immersion in SBF, likely because of their biomimetic architectures mimicking natural bone. This study has shown that powder bed fusion processes can be used to fabricate scaffolds with controlled rates of strength degradation and bone regeneration by selecting appropriate architecture and bioactive glass composition. These scaffolds can be used to repair specific regions of trabecular bone, based on functional requirements. Cubic and diamond scaffolds with ~50% porosity and ~1 mm pore size were used to treat a full-thickness 4.6 mm diameter rat calvarial defect with or without BMP-2. There was no significant difference in mineralized bone formation for defects treated with cubic and diamond architectures after 6 weeks of implantation. However, a higher percentage of fibrous connective tissue and high osteoblast activity was observed in the defects treated with diamond scaffolds. The addition of BMP-2 significantly increased the bone regeneration from 6% (without BMP-2) to 40% of the defect area.

Acknowledgments

The glasses used in this work were provided by Mo-Sci Corporation, Rolla, MO. Authors thank Natalie Holl for help on technical editing and acknowledge the assistance of Jacob Mendez and Bradley Bromet for image analysis.

References

1. Jones JR, 2013, Review of Bioactive Glass: From Hench to Hybrids. *Acta Biomater*, 9:4457–86.
2. Hench LL, 2006, The Story of Bioglass®. *J Mater Sci Mater Med*, 17:967–78.
3. Greenspan D, 2019, Bioglass at 50-A Look at Larry Hench's Legacy and Bioactive Materials. *Biomed Glas*, 5:178–84. DOI: 10.1515/bglass-2019-0014.
4. Rahaman MN, Day DE, Bal BS, *et al*., 2011, Bioactive Glass in Tissue Engineering. *Acta Biomater*, 7:2355–73.
5. Fu Q, Rahaman MN, Fu H, *et al*., 2010, Silicate, Borosilicate, and Borate Bioactive Glass Scaffolds with Controllable Degradation Rate for Bone Tissue Engineering Applications. I. Preparation and *In Vitro* Degradation. *J Biomed Mater Res Part A*, 95A:164–71. DOI: 10.1002/jbm.a.32824.
6. Jung S, Day D, 2009, Conversion Kinetics of Silicate, Borosilicate, and Borate Bioactive Glasses to Hydroxyapatite. *Phys Chem Glas*, 50:85–8.
7. Balasubramanian P, Kolzow J, Chen RR, *et al*., 2018, Boron-containing Bioactive Glasses in Bone and Soft Tissue Engineering. *J Eur Ceram Soc*, 38:855–69.
8. Yuan S, Shen F, Chua CK, *et al*., 2019, Polymeric Composites for Powder-based Additive Manufacturing: Materials and Applications. *Prog Polym Sci*, 91:141–68.
9. Ng WL, Lee JM, Zhou M, *et al*., 2020, Vat Polymerization-based Bioprinting Process, Materials, Applications and Regulatory Challenges IOP Science. *Biofabrication*, 12:022001. DOI: 10.1088/1758-5090/ab6034.
10. Goh GD, Yap YL, Tan HK, *et al*., 2020, Process Structure Properties in Polymer Additive Manufacturing via Material Extrusion: A Review. *Crit Rev Solid State Mater Sci*, 45:113–33. DOI: 10.1080/10408436.2018.1549977.
11. Cai S, Xi J, 2008, A Control Approach for Pore Size Distribution in the Bone Scaffold Based on the Hexahedral Mesh Refinement. *CAD Comput Aided Des*, 40:1040–50. DOI: 10.1016/j.cad.2008.09.004.
12. Melchels FP, Bertoldi K, Gabbrielli R, *et al*., 2010, Mathematically Defined Tissue Engineering Scaffold Architectures Prepared by Stereolithography. *Biomaterials*, 31:6909–16. DOI: 10.1016/j.biomaterials.2010.05.068.
13. Challis VJ, Roberts AP, Grotowski JF, *et al*., 2010, Prototypes for Bone Implant Scaffolds Designed via Topology Optimization and Manufactured by Solid Freeform Fabrication. *Adv Eng Mater*, 12:1106–10. DOI: 10.1002/adem.201000154.
14. Feng J, Fu J, Li Z, *et al*., 2018, A Review of the Design Methods of Complex Topology Structures for 3D Printing. *Vis Comput Ind Biomed Art*, 1:5.
15. Wang G, Shen L, Zhao J, *et al*., 2018, Design and Compressive Behavior of Controllable Irregular Porous Scaffolds: Based on Voronoi-Tessellation and for Additive Manufacturing. *ACS Biomater Sci Eng*, 4:719–27. DOI: 10.1021/acsbiomaterials.7b00916.
16. Ng WL, Chua CK, Shen YF, *et al*., 2019, Print Me An Organ! Why We Are Not There Yet. *Prog Polym Sci*, 97:101145.

DOI: 10.1016/j.progpolymsci.2019.101145.

17. Sing SL, Yeong WY, Wiria FE, *et al*., 2017, Direct Selective Laser Sintering and Melting of Ceramics: A Review. *Rapid Prototyp J*, 23:611–23. DOI: 10.1108/rpj-11-2015-0178.
18. Datsiou KC, Saleh E, Spirrett F, *et al*., 2019, Additive Manufacturing of Glass with Laser Powder Bed Fusion. *J Am Ceram Soc*, 102:4410–4. DOI: 10.1111/jace.16440.
19. Yves-Christian H, *et al*., 2010, Net Shaped High Performance Oxide Ceramic Parts by Selective Laser Melting. In: Physics Procedia. Vol. 5. Elsevier B.V., Berlin, pp. 587–94. DOI: 10.1016/j.phpro.2010.08.086.
20. Verga F, Mario B, Laura C, *et al*., 2020, Laser-based Powder Bed Fusion of Alumina Toughened Zirconia. *Addit Manuf*, 31:100959. DOI: 10.1016/j.addma.2019.100959.
21. Kolan KC, Leu MC, Hilmas GE, *et al*., 2011, Fabrication of 13-93 Bioactive Glass Scaffolds for Bone Tissue Engineering Using Indirect Selective Laser Sintering. *Biofabrication*, 3:025004. DOI: 10.1088/1758-5082/3/2/025004.
22. Goodridge RD, Dalgarno KW, Wood DJ, *et al*., 2006, Indirect Selective Laser Sintering of an Apatite-mullite Glass-Ceramic for Potential Use in Bone Replacement Applications. *Proc Inst Mech Eng Part H J Eng Med*, 220:57–68. DOI: 10.1243/095441105x69051.
23. Van Bael S, Chai YC, Truscello S, *et al*., 2012, The Effect of Pore Geometry on the *In Vitro* Biological Behavior of Human Periosteum-Derived Cells Seeded on Selective Laser-melted Ti6Al4V Bone Scaffolds. *Acta Biomater*, 8:2824–34. DOI: 10.1016/j.actbio.2012.04.001.
24. Zadpoor AA, 2015, Bone Tissue Regeneration: The Role of Scaffold Geometry. *Biomater Sci*, 3:231–45. DOI: 10.1039/c4bm00291a.
25. Ouyang P, Dong H, He X, *et al*., 2019, Hydromechanical Mechanism behind the Effect of Pore Size of Porous Titanium Scaffolds on Osteoblast Response and Bone Ingrowth. *Mater Des*, 183:108151. doi.org/10.1016/j.matdes.2019.108151.
26. Gariboldi MI, Best SM, 2015, Effect of Ceramic Scaffold Architectural Parameters on Biological Response. *Front Bioeng Biotechnol*, 3:151. DOI: 10.3389/fbioe.2015.00151.
27. Roosa SM, Kemppainen JM, Moffitt EN, *et al*., 2010, The Pore Size of Polycaprolactone Scaffolds has Limited Influence on Bone Regeneration in an *In Vivo* Model. *J Biomed Mater Res Part A*, 92:359–68. DOI: 10.1002/jbm.a.32381.
28. Perez RA, Mestres G, 2016, Role of Pore Size and Morphology in Musculo-skeletal Tissue Regeneration. *Mater Sci Eng C*, 61:922–39. DOI: 10.1016/j.msec.2015.12.087.
29. Lin Y, Liu X, Xiao W, *et al*., 2015, Long-term Bone Regeneration, Mineralization and Angiogenesis in Rat Calvarial Defects Implanted with Strong Porous Bioactive Glass (13-93) Scaffolds. *J Non Cryst Solids*, 432:4–13. DOI: 10.1016/j.jnoncrysol.2015.04.008.
30. Bi L, Jung S, Day D, *et al*., 2012, Evaluation of Bone Regeneration, Angiogenesis, and Hydroxyapatite Conversion in Critical-sized Rat Calvarial Defects Implanted with Bioactive Glass Scaffolds. *J Biomed Mater Res Part A*, 100A:3267–75. DOI: 10.1002/jbm.a.34272.
31. Bidan CM, Kommareddy KP, Rumpler M, *et al*., 2013, Geometry as a Factor for Tissue Growth: Towards Shape Optimization of Tissue Engineering Scaffolds. *Adv Healthc Mater*, 2:186–94. DOI: 10.1002/adhm.201200159.
32. Bidan CM, Kommareddy KP, Rumpler M, *et al*., 2012, How Linear Tension Converts to Curvature: Geometric Control of Bone Tissue Growth. *PLoS One*, 7:e36336. DOI: 10.1371/journal.pone.0036336.
33. Rumpler M, Woesz A, Dunlop JW, *et al*., 2008, The Effect of Geometry on Three-dimensional Tissue Growth. *J R Soc Interface*, 5:1173–80.
34. Kolan KC, Thomas A, Leu MC, *et al*., 2015, *In Vitro* Assessment of Laser Sintered Bioactive Glass Scaffolds with Different Pore Geometries. *Rapid Prototyp J*, 21:152–8. DOI: 10.1108/rpj-12-2014-0175.
35. Kolan KC, Leu MC, Hilmas GE, *et al*., 2012, Effect of Material, Process Parameters, and Simulated Body Fluids on Mechanical Properties of 13-93 Bioactive Glass Porous Constructs Made by Selective Laser Sintering. *J Mech Behav Biomed Mater*, 13:14–24. DOI: 10.1016/j.jmbbm.2012.04.001.
36. Kokubo T, Takadama H, 2006, How Useful is SBF in Predicting *In Vivo* Bone Bioactivity? *Biomaterials*, 27:2907–15. DOI: 10.1016/j.biomaterials.2006.01.017.
37. Schindelin J, Arganda-Carreras I, Frise E, *et al*., 2012, Fiji: An Open-source Platform for Biological-image Analysis. *Nat Methods*, 9:676–82. DOI: 10.1038/nmeth.2019.
38. Melchels FP, Barradas AM, van Blitterswijk CA, *et al*., 2010, Effects of the Architecture of Tissue Engineering Scaffolds on Cell Seeding and Culturing. *Acta Biomater*, 6:4208–17. DOI: 10.1016/j.actbio.2010.06.012.
39. Carter DR, Hayes WC, 1976, Bone Compressive Strength: The Influence of Density and Strain Rate. *Science*, 194:1174–6. DOI: 10.1126/science.996549.
40. Wu D, Isaksson P, Ferguson SJ, *et al*., 2018, Young's Modulus of Trabecular Bone at the Tissue Level: A Review. *Acta Biomater*, 78:1–12. DOI: 10.1016/j.actbio.2018.08.001.
41. Freitas GP, Lopes HB, Souza AT, *et al*., 2019, Cell Therapy: Effect of Locally Injected Mesenchymal Stromal Cells

Derived from Bone Marrow or Adipose Tissue on Bone Regeneration of Rat Calvarial Defects. *Sci Rep*, 9:13476. DOI: 10.1038/s41598-019-50067-6.

42. Gibson LJ, Ashby MF, 1982, The Mechanics of Three-Dimensional Cellular Materials. *Proc R Soc A Math Phys Sci*, 382:43–59.
43. Ryshkewitch E, 1953, Compression Strength of Porous Sintered Alumina and Zirconia. *J Am Ceram Soc*, 36:65–8.
44. Duckworth W, 1953, Discussion of Ryshkewitch Paper. *J Am Ceram Soc*, 36:68.
45. Rice RW, 1996, Evaluation and Extension of Physical Property-porosity Models Based on Minimum Solid Area. *J Mater Sci*, 31:102–18.
46. Hattiangadi A, Bandyopadhyay A, 2000, Strength Degradation of Nonrandom Porous Ceramic Structures under Uniaxial Compressive Loading. *J Am Ceram Soc*, 83:2730–6. DOI: 10.1111/j.1151-2916.2000.tb01624.x.
47. Rice RW, 1993, Comparison of Stress Concentration Versus Minimum Solid Area Based Mechanical Property-porosity Relations. *J Mater Sci*, 28:2187–90. DOI: 10.1007/bf00367582.
48. Deliormanl AM, 2012, *In Vitro* Assessment of Degradation and Bioactivity of Robocast Bioactive Glass Scaffolds in Simulated Body Fluid. *Ceram Int*, 38:6435–44. DOI: 10.1016/j.ceramint.2012.05.019.
49. Deliormanli AM, Rahaman MN, 2012, Direct-write Assembly of Silicate and Borate Bioactive Glass Scaffolds for Bone Repair. *J Eur Ceram Soc*, 32:3637–46. DOI: 10.1016/j.jeurceramsoc.2012.05.005.
50. Kolan KC, Semon J, Bromet B, *et al*., 2019, Bioprinting with Human Stem Cells-laden Alginate-gelatin Bioink and Bioactive Glass for Tissue Engineering. *Int J Bioprint*, 5:3. DOI: 10.18063/ijb.v5i2.2.204.
51. Murphy C, Kolan K, Li W, *et al*., 2017, 3D Bioprinting of Stem Cells and Polymer/Bioactive Glass Composite Scaffolds for Tissue Engineering. *Int J Bioprinting*, 3:54–64. DOI: 10.18063/ijb.2017.01.005.
52. Hustedt JW, Blizzard DJ, 2018, The Controversy Surrounding Bone Morphogenetic Proteins in the Spine: A Review of Current Research. In: Getting to Good: Research Integrity in the Biomedical Sciences. Vol. 87. Springer International Publishing, Basel, Switzerland, pp. 9–22.
53. Carragee EJ, Chu G, Rohatgi R, *et al*., 2013, Cancer Risk After Use of Recombinant Bone Morphogenetic Protein-2 for Spinal Arthrodesis. *J Bone Joint Surg Am*, 95:1537–45. DOI: 10.1016/j.spinee.2013.11.026.
54. Injamuri S, Rahaman MN, Shen Y, *et al*., 2020, Relaxin Enhances Bone Regeneration with BMP-2-Loaded Hydroxyapatite Microspheres. *J Biomed Mater Res Part A*, 108:1231–42. DOI: 10.1002/jbm.a.36897.
55. Gu Y, Bal B, Rahaman N, *et al*., 2015, *In Vivo* Evaluation of Scaffolds with a Grid-Like Microstructure Composed of a Mixture of Silicate (13-93) and Borate (13-93B3) Bioactive Glasses. John Wiley and Sons, Inc., New York, pp. 53–64. DOI: 10.1002/9781119040392.ch6.
56. Karageorgiou V, Kaplan D, 2005, Porosity of 3D Biomaterial Scaffolds and Osteogenesis. *Biomaterials*, 26:5474–91. DOI: 10.1016/j.biomaterials.2005.02.002.
57. Sopyan I, Gunawan, 2013, Development of Porous Calcium Phosphate Bioceramics for Bone Implant Applications: A Review. *Recent Patents Mater Sci*, 6:238–52. DOI: 10.2174/18744648113069990012.
58. Gu Y, Huang W, Rahaman MN, *et al*., 2013, Bone Regeneration in Rat Calvarial Defects Implanted with Fibrous Scaffolds Composed of a Mixture of Silicate and Borate Bioactive Glasses. *Acta Biomater*, 9:9126–36. DOI: 10.1016/j.actbio.2013.06.039.
59. Bi L, Zobell B, Liu X, *et al*., 2014, Healing of Critical-size Segmental Defects in Rat Femora Using Strong Porous Bioactive Glass Scaffolds. *Mater Sci Eng C*, 42:816–24. DOI: 10.1016/j.msec.2014.06.022.
60. Wang H, Zhao S, Xiao W, *et al*., 2015, Three-dimensional Zinc Incorporated Borosilicate Bioactive Glass Scaffolds for Rodent Critical-sized Calvarial Defects Repair and Regeneration. *Colloids Surfaces B Biointerfaces*, 130:149–56. DOI: 10.1016/j.colsurfb.2015.03.053.
61. Wang H, Zhao S, Zhou, J, *et al*., 2014, Evaluation of Borate Bioactive Glass Scaffolds as a Controlled Delivery System for Copper Ions in Stimulating Osteogenesis and Angiogenesis in Bone Healing. *J Mater Chem B*, 2:8547–57. DOI: 10.1039/c4tb01355g.
62. Hart NH, Nimphius S, Rantalainen T, *et al*., 2017, Mechanical Basis of Bone Strength: Influence of Bone Material, Bone Structure and Muscle Action. *J Musculoskelet Neuronal Interact*, 17:114–39.